



Steam-driven crystalline-amorphous coupling design of homogenous metal hydroxides for oxygen evolution reaction

Jinjiang Gao¹, Chen Qiu¹, Min Ju, Simeng Li, Rongxing Yu, Hongzhi Liu, Mingyu Hu, Jun Yu, Mei Hong*, Shihe Yang*

State Key Laboratory of Chemical Oncogenomics, Guangdong Provincial Key Laboratory of Nano-Micro Materials Research, School of Chemical Biology & Biotechnology, Peking University Shenzhen Graduate School (PKUSZ), Shenzhen 518055, PR China

ARTICLE INFO

Keywords:

Electrocatalysis
Oxygen evolution reaction
Crystalline–amorphous coupling
Methanol steam
Stability

ABSTRACT

The crystalline-amorphous (c-a) structure is emerging as a promising design of oxygen evolution electrocatalysts. However, homogenous compositions and excellent stability are hindering further industrial applications. Only by using metal nitrates and methanol solvent, we provide an effective steam-driven strategy to directly fabricate c-a electrocatalysts. The division of methanol molecules establishes an experimental approach to analyze the targeted transformation from crystalline to c-a phase for monometallic nickel hydroxy-nitrates. Following, this design is successfully extended to the bimetallic NiFe layered double hydroxide (NiFe-LDH). The presence of Fe³⁺ not only effectively promotes electrochemical activity but also enhances adhesion to the nickel foam, conjuring up an ultra-active and ultra-stable NiFe_{A-S}@NF electrocatalyst with an overpotential of 205 mV at 10 mA cm⁻² and excellent 200 h stability at 500–1000 mA cm⁻². In light of the above findings and preliminary scale-up experiment, this approach offers both fundamental and practical guidelines for other non-noble-metal-based electrocatalysts.

1. Introduction

Electrocatalytic water splitting is regarded as a promising technology for addressing serious energy and environmental crises, and has been actively pursued in recent decades [1,2]. The practical application of this technology is limited in part by oxygen evolution reaction (OER) [3,4]. Even with noble metal catalysts (RuO₂ and IrO₂), a substantial overpotential is required to overcome the sluggish OER kinetics [5,6]. To date, efficient non-noble-metal-based catalysts have been the research target [7–9]. Ingenious design strategies have been proposed to provide guidance for a higher activity including compositional modulation [10], suitable supports [11,12], nanostructure design [13,14], and lattice strain engineering [15]. Experimental and theoretical studies have already demonstrated that inexpensive catalysts can obtain lower overpotentials than commercial catalysts [16–18]. Besides activity, the durability of equal importance directly impacts a catalyst's cost-effectiveness [19]. To reach a practical level of large-scale applications, an OER electrocatalyst is required to sustain extremely large current densities over a long period [20,21].

Owing to the advantageous isotropy and the dynamic re-assembly of amorphous phase, transformations from crystalline to amorphous structures have been applied to tune the physicochemical properties and optimize catalytic performance of catalysts [22–24]. Characterized by the short-range order and long-range disorder, heterogeneous crystalline-amorphous (c-a) structures have attracted increasing attention as a promising design for OER catalysts [25–27]. Compared to their crystalline counterparts, the incorporation of amorphous phase is crucial for achieving optimal reaction structure [28]. For example, Li et al. [29] reported a synchronous synthetic strategy to obtain a c-a structure consisting of crystalline metallic Ag and amorphous NiCoMo oxides on nickel foam. Liang et al. [30] developed NiFe alloy (core)–ultrathin amorphous oxyhydroxide (shell) nanowire arrays using a magnetic field assisted chemical deposition method, which were used as exceptionally active OER electrodes. In addition, surface amorphization could also produce a high-density of c-a interfaces of metal-metalloids [31]. Despite many efforts, most of the c-a structures that have been fabricated to date are composed of different compositions. The difficulties involved in obtaining a homogeneous composition have been

* Corresponding authors.

E-mail addresses: hongmei@pku.edu.cn (M. Hong), chsyang@pku.edu.cn (S. Yang).

¹ These authors contributed equally

related to unbalanced, uncontrollable and unstable growth of the hetero-phases. It stands to reason that ideal c-a structures with a homogeneous chemical composition should be an interesting albeit challenging pursuit.

In this work, nickel element, one of the most common non-precious components, is chosen as the starting point. We first demonstrate that c-a nanosheets can be directly formed from monometallic nickel nitrate with the assistance of methanol steam. Based on our deliberate division of methanol molecules, the neat crystalline structure of $\text{Ni}_3(\text{NO}_3)_2(\text{OH})_4$ can be flexibly transformed into a c-a coupling structure. Spatially interrupted growth caused by methanol molecules promotes the synchronous formation of c-a hetero-phases with intimate contacts. Following this design, we identify the important role of Fe^{3+} for operating bimetallic NiFe layered double hydroxide (NiFe-LDH). Comprehensive electrochemical measurements including operando Raman and electrochemical quartz crystal microbalance with dissipation (EQCM-D) systematically analyze the beneficial activation process. Thus, the methanol steam-driven coupling is a viable route to design ultra-stable and efficient electrocatalysts.

2. Experimental section

2.1. Synthesis of Ni@CC and Ni@NF

580 mg $\text{Ni}(\text{NO}_3)_2 \cdot 6\text{H}_2\text{O}$ was dissolved in 15 mL methanol, and was ultrasonicated for 20 min. Next, small pieces of carbon cloth (CC) were immersed into the precursor solution. After suitable ultrasonic treatment, three different pretreatments were chosen to separate adsorbed methanol and surrounding methanol. The first one was dried by an infrared lamp (about 3 min), and then placed into a 100 mL Teflon-lined autoclave; In the second procedure, the Teflon holder with the immersed CC was placed into a 100 mL autoclave; In the third procedure, the immersed CC was also placed into a 100 mL autoclave but with 15 mL methanol at the bottom of the Teflon liner. Next, the autoclave was heated to 180 °C for 10 h. Here, the samples synthesized by the different procedures are named as $\text{Ni}_\text{D}@\text{CC}$, $\text{Ni}_\text{A}@\text{CC}$ and $\text{Ni}_{\text{A-S}}@\text{CC}$, respectively. Using the similar procedures, nickel foam (NF) was used to grow $\text{Ni}_\text{D}@\text{NF}$, $\text{Ni}_\text{D}@\text{NF-2}$, $\text{Ni}_\text{A}@\text{NF}$ and $\text{Ni}_{\text{A-S}}@\text{NF}$. Here, to change the amount of adsorbed methanol and residual water, $\text{Ni}_\text{D}@\text{NF}$ and $\text{Ni}_\text{D}@\text{NF-2}$ were dried for 10 min and 5 min, respectively.

2.2. Synthesis of $\text{Fe}_{\text{A-S}}@\text{CC}$, $\text{NiFe}_{\text{A-S}}@\text{CC}$ and $\text{NiFe}_{\text{A-S}}@\text{NF}$

1616 mg $\text{Fe}(\text{NO}_3)_3 \cdot 9\text{H}_2\text{O}$ was dissolved in 20 mL methanol. After being ultrasonicated for 10 min, the precursor solution could be obtained for the fabrication of $\text{Fe}_{\text{A-S}}@\text{CC}$ using the same synthesis procedures of $\text{Ni}_{\text{A-S}}@\text{CC}$. 580 mg $\text{Ni}(\text{NO}_3)_2 \cdot 6\text{H}_2\text{O}$ and 1616 mg $\text{Fe}(\text{NO}_3)_3 \cdot 9\text{H}_2\text{O}$ were mixed in a beaker with 20 mL methanol, and then was ultrasonicated for 20 min to obtain a homogeneous precursor solution. The preparation was similar except that the precursor solution contained both nickel and iron with Ni:Fe molar ratio of 1:2. Depending on the type of supports, the samples were labeled as $\text{NiFe}_{\text{A-S}}@\text{CC}$ and $\text{NiFe}_{\text{A-S}}@\text{NF}$. To explore the influence of Fe^{3+} , we also increased the ratio of Ni: Fe to 1:1, which is labeled as $\text{NiFe}_{\text{A-S}}@\text{CC}$ (1:1). Preliminary scale-up experiment was finished by using enlarged supports and devices, including larger nickel foam (4×5 cm), bigger Teflon liner, more precursor solution, and 500 mL autoclave.

2.3. Characterizations

The X-ray diffraction (XRD) characterization was carried on a Rigaku D/Max-2200 PC diffractometer at 40 kV/40 mA with Cu K radiation ($\lambda = 1.5418$ Å). Scanning electron microscope (SEM, ZEISS SUPRA 55) pattern was recorded to identify different morphologies. The transmission electron microscopy (TEM), high resolution TEM (HRTEM) and electron diffraction pattern were performed on a JEM3200FS field

emission source transmission electron microscope. The surface wettability was investigated by contact angle measuring instrument (MDTC-EQ-M07-01). X-ray photoelectron spectroscopy (XPS) spectra were collected on Thermo ESCALAB 250Xi (Thermo Fisher). Elemental contents of the nanosheets were confirmed by inductively coupled plasma optical emission spectroscopy (ICP-OES, Agilent 5100). The in-situ Raman was performed on a Horiba LabRAM HR800 Evolution Raman microscope using a 532 nm laser. The X-ray absorption fine structure spectra (Ni K-edge) were collected at 4B9A beamline in Beijing Synchrotron Radiation Facility (BSRF). The storage rings of BSRF was operated at 2.5 GeV with a stable current of 400 mA. Using Si(III) double-crystal monochromator, the data collection was carried out in fluorescence mode using Lytle detector.

2.4. Electrochemical measurements

Electrochemical measurements were conducted with electrochemical working stations (CHI 760E, Gamry reference 3000) in a standard three electrode system (Teflon electrolytic cell, 1 M KOH). Platinum sheet or graphite rod and Hg/HgO electrode were utilized as the counter and reference electrode. Here, the Randles-Sevcik equation is used to analyze the peak current i_p (A) fluctuations as follows: $i_p = 0.446nFAC^0(nFvD_0/RT)^{1/2}$. Where n is the number of electrons transferred in the redox event, F is Faraday's constant, R is the universal gas constant, T is the temperature, A (cm^2) is the electrode surface area, v (V s^{-1}) is the scan rate, D_0 ($\text{cm}^2 \text{s}^{-1}$) is the diffusion coefficient of the oxidized analyte, and C^0 (mol cm^{-3}) is the concentration of the analyte.

The cyclic voltammetry (CV) measurements were cycled at a scan rate of 10 mV/s. From high initial potentials to low final potentials. Linear sweep voltammetry (LSV) measurements were conducted with a 5 mV/s scan rate, and presented without iR compensation. Tafel slope was directly calculated from LSV curves. Electrochemical impedance spectroscopy (EIS) analysis were conducted from 10 kHz to 0.05 Hz at 0.60 V vs. Hg/HgO for $\text{Ni}_{\text{A-S}}@\text{NF}$, and at 0.55 V vs. Hg/HgO for $\text{NiFe}_{\text{A-S}}@\text{NF}$, respectively. The ECSA was determined by measuring the capacitive current associated with double-layer charging. Here, the cyclic voltammograms (CVs) are obtained in non-Faradaic region (0.01–0.11 V vs. Hg/HgO) at various scan rates (10–200 mV/s). C_{dl} is extracted by plotting $(j_a - j_c)/2$ versus scan rate, where j_a and j_c are the anode and cathode current densities, respectively. Chronopotentiometry measurements were performed to evaluate the long-term stability under a constant current density of 200 mA cm^{-2} , 500 mA cm^{-2} , and 1000 mA cm^{-2} . To mimic the industrial operating conditions, the further condition was conducted at 85 °C under 500 mA cm^{-2} with 6 M KOH as electrolyte. Potentials in this work were converted to reversible hydrogen electrode (RHE) based on the equation of E (vs RHE) = E (vs Hg/HgO) + 0.0591 pH + 0.098 V.

The electrochemical quartz crystal microbalance with dissipation (EQCM-D) measurements were performed on a Q-Sense from Biolin Scientific. The gold sensors coated with powder from $\text{NiFe}_{\text{A-S}}@\text{NF}$, Ag/AgCl and Pt were acted as working, reference and counter electrodes, respectively. CV cycles were set at a scan rate of 2 mV/s. The changes of crystal resonant frequency, $\Delta f/n$, is a linear function of Sauerbrey mass depending only on the mechanical properties of the quartz crystal plate. By monitoring changes of the resonance frequency, Δf , it is possible to detect small operando mass changes of powder- $\text{NiFe}_{\text{A-S}}@\text{NF}$ upon the electrochemical CV cycles. The dissipation (ΔD) gives information about the energy losses in the system and are particularly useful in the study of layer properties. For an AT-cut, 5 MHz quartz crystal, $C = 17.7 \text{ ng/cm}^2 \text{ Hz}$. The Sauerbrey mass (ng/cm^2) can be calculated as follows: $M = -C \bullet \Delta f/n$. Where Δf is the co-frequency and n is the harmonic number.

3. Results and discussion

3.1. Conversion mechanism and extension to bimetallic NiFe-precursor solution

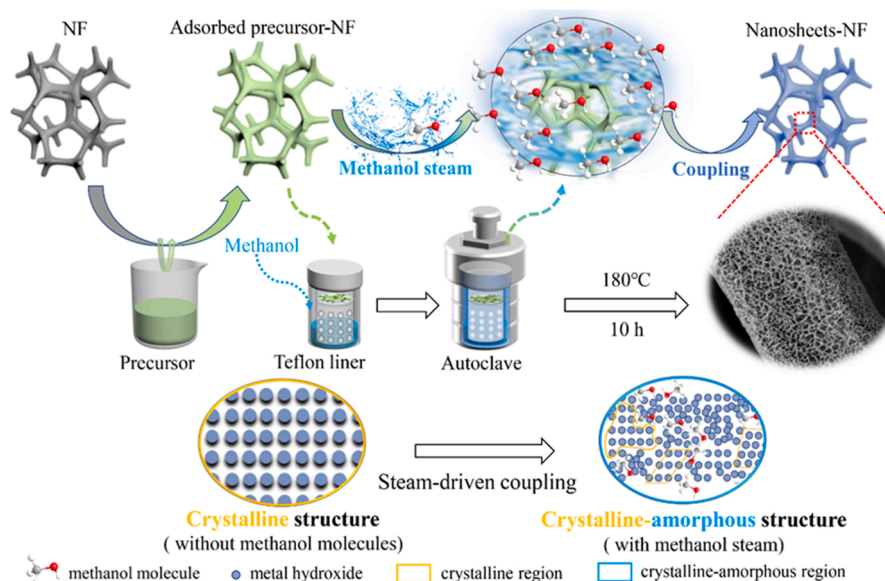
The methanol steam-driven c-a coupling strategy is illustrated in Scheme 1. In order to avoid distraction, the analysis is firstly focused on monometallic Ni precursor solution grown on CC. Inspired by crystal-phase engineering, the experimental design is carefully planned to make out the role of methanol molecules under the following three conditions: (1) without any methanol in the system, (2) only with adsorbed methanol, and (3) with adsorbed and surrounding methanol. Interestingly, three different conditions closely related to the states of methanol molecules have a dramatic effect on the morphology and chemical composition. After the treatment with an infrared lamp, methanol molecules remaining on the surface of CC are expected to be minimal. The morphology of $\text{Ni}_D\text{@CC}$ is shown in Fig. 1a and obviously, randomly orientated nanobelts deposit on the surface of CC. Fig. 2a presents the XRD pattern of $\text{Ni}_D\text{@CC}$, which perfectly matches the standard pattern of PDF#27-0939. Thereinto, five strong diffraction peaks located at 10.95° , 13.69° , 16.68° , 20.74° and 21.98° can be indexed to the (200), (002), (102), (202) and (400) planes of the monoclinic crystal $\text{Ni}_2(\text{NO}_3)_2(\text{OH})_2 \cdot 2\text{H}_2\text{O}$, respectively. Differently, $\text{Ni}_A\text{@CC}$ obtained from undried precursor solution-CC without adding bottom methanol displays flake-like hexagonal crystal habit (Fig. 1b). Except for the monoclinic crystal diffraction peaks, the diffraction peaks at 12.82° , 25.80° , 33.01° and 35.55° match well with the (001), (002), (100) and (101) planes of $\text{Ni}_3(\text{NO}_3)_2(\text{OH})_4$ (PDF#22-0752), respectively. By providing abundant methanol steam, above-mentioned thick hexagonal sheets were transformed into ultrathin nanosheets (Fig. 1c). Generally, nickel hydroxy-nitrates have considerably sharper diffraction peaks. With this precise adjustment, the diffraction peaks of $\text{Ni}_A\text{S@CC}$ in Fig. 2a indicate obvious signal of amorphous part, and the crystalline peaks only index to PDF#22-0752.

When the same precursor solution was used on NF, similar phenomena occurred (Fig. 1d-f). However, due to the rougher surface, NF could adsorb more precursor solution than CC. As for $\text{Ni}_D\text{@NF}$, the adsorbed Ni source could completely consume the residual water molecules. So, the XRD pattern of peeled powder directly matches well with diffraction peaks of $\text{Ni}_3(\text{NO}_3)_2(\text{OH})_4$ (PDF#22-0752), without any other diffraction peaks (Fig. 2b). To verify our conjecture about water molecules, we decreased the drying time for $\text{Ni}_D\text{@NF}$. As indicated in the

XRD pattern of powder- $\text{Ni}_D\text{@NF}$ -2 (Fig. S1a), more water molecules led to the appearance of characteristic peaks of $\text{Ni}_2(\text{NO}_3)_2(\text{OH})_2 \cdot 2\text{H}_2\text{O}$. $\text{Ni}_A\text{S@NF}$ does not show any other XRD peaks except three diffraction peaks of NF at 44.5° , 51.8° and 76.4° , further confirming the presence of amorphous structure (Fig. S1b). In addition, Fig. S2 reveals that Ni, N, and O elements are uniformly dispersed across the interconnected nanomaterials.

Having established the realistic structure of layered materials, we now use these structures to decipher how to produce thin-nanosheets. As shown in Fig. 1b-c, $\text{Ni}_A\text{S@CC}$ exhibits a thickness of about 12 nm, much thinner than that of the bulk $\text{Ni}_A\text{@CC}$ (about 50 nm). By implementing our design, the solvent steam interruption occurred simultaneously during the formation of nickel hydroxy-nitrates. Condensation of residual water molecules, running during the hydrolysis, resulted in the formation of the respective structures. On the other hand, it should be pointed out that part adsorbed water molecules inevitably co-evaporate with the leaving high-temperature methanol molecules. Therefore, adjustable nickel hydroxy-nitrates, which can be hydrated, have the general formula $\text{Ni}(\text{OH})_{2-x}(\text{NO}_3)_x \cdot n\text{H}_2\text{O}$, such as $\text{Ni}_A\text{@CC}$ and $\text{Ni}_D\text{@NF}$ -2. Different from α -nickel hydroxide, the nitrate ions are strongly grafted to the nickel hydroxide sheets. However, high-temperature methanol molecules can impact or inhibit the formation of ionic bonds and hydrogen bonds, and then directly restrain the Z-direction growth of host layers. Correspondingly, the trend of thickness fluctuations also applies to $\text{Ni}_D\text{@NF}$, $\text{Ni}_A\text{@NF}$ and $\text{Ni}_A\text{S@NF}$ (Fig. 1d-f). Based on the above, the content of residual water molecules determines if the hydrate specie could exist with nickel nitrate hydroxides, while the methanol steam plays an important role in morphology control towards nanosheet arrays.

To unravel the transformation process of crystalline structure, $\text{Ni}_D\text{@NF}$ and $\text{Ni}_A\text{S@NF}$ with the same chemical composition ($\text{Ni}_3(\text{NO}_3)_2(\text{OH})_4$) were chosen under two extreme reaction situations. From the high-resolution TEM image (HRTEM, Fig. 2c) of powder scratched off from $\text{Ni}_D\text{@NF}$, the crystalline part takes an overwhelming majority, which is in line with the obvious spots in selected area electron diffraction (SAED) pattern and XRD peaks (Fig. 2b). The sheets of $\text{Ni}_D\text{@NF}$ are stacked together in a highly ordered fashion. Measured distances of distinct lattice fringes are 0.21 and 0.25 nm, matching well with the (102) and (101) facets of $\text{Ni}_3(\text{NO}_3)_2(\text{OH})_4$, respectively. So, the inability to effectively circulate methanol molecules and the condensation reaction of residual water molecules finished the crystalline closed-loop. As for the opposite extreme situation with both adsorbed and



Scheme 1. Schematic illustration of the methanol steam-driven c-a coupling strategy.

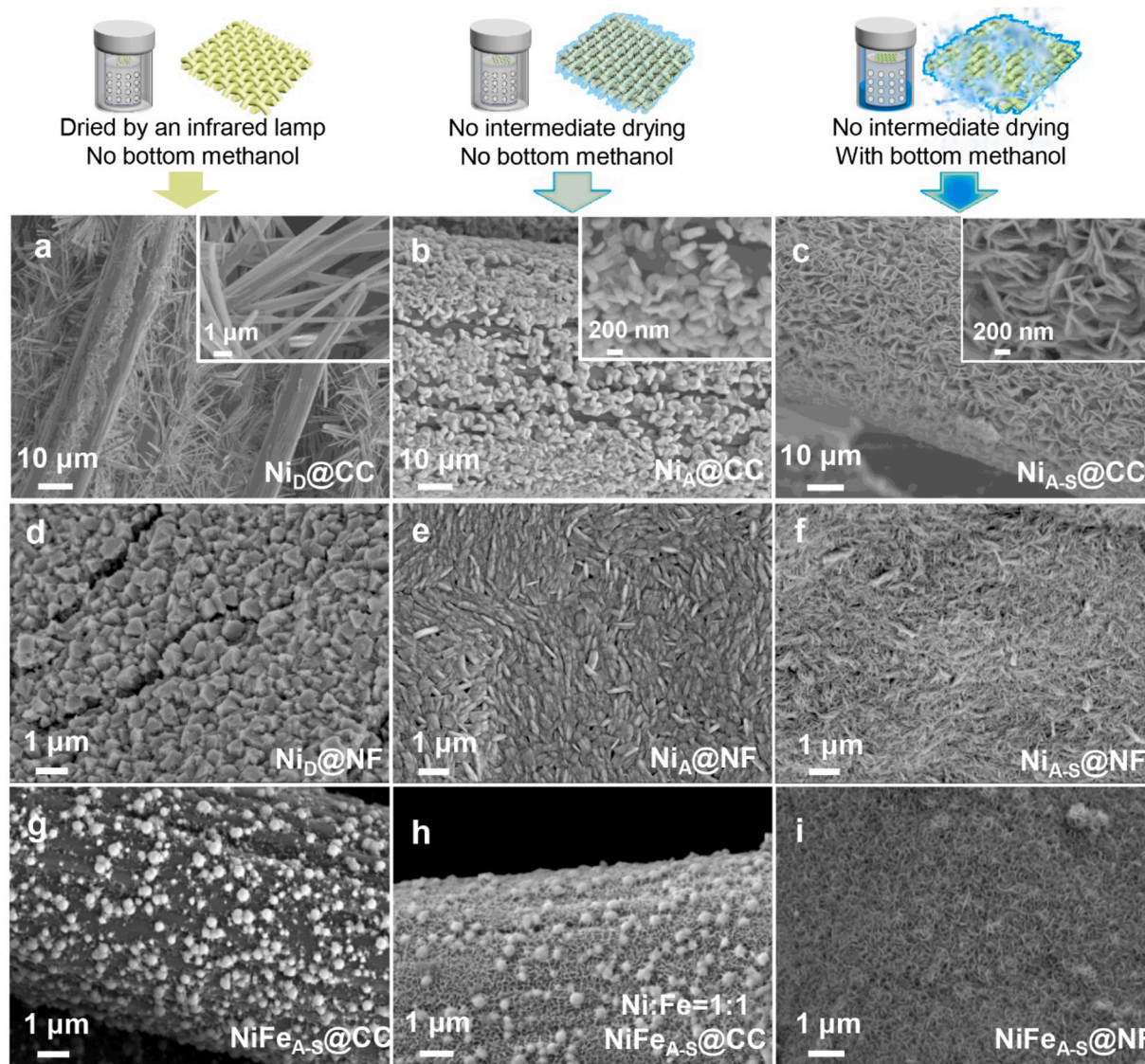


Fig. 1. Top row: Sketch of the designed conditions with different combination of adsorbed methanol and surrounding methanol. Comparative SEM images of (a) $\text{Ni}_D@CC$, (b) $\text{Ni}_A@CC$, (c) $\text{Ni}_{A-S}@CC$, (d) $\text{Ni}_D@NF$, (e) $\text{Ni}_A@NF$, (f) $\text{Ni}_{A-S}@NF$, (g) $\text{NiFe}_{A-S}@CC$, (h) $\text{NiFe}_{A-S}@CC$ (Ni:Fe=1:1) and $\text{NiFe}_{A-S}@NF$.

bottom methanol solvent, the powder of $\text{Ni}_{A-S}@NF$ contains easily distinguishable amorphous structure observed in HRTEM images of Fig. S3a and Fig. 2d. The lattice fringes with a spacing of about 0.26 nm corresponding to the (101) plane are constantly interrupted by numerous amorphous domains. Except for the short-range order state, fluctuating distances in the inverse FFT lattice image indicate the existence of lattice distortion. In general, if the transformation happened after the finished crystallization process, the pristine catalyst should entirely transform into an amorphous structure within sufficiently long synthesis time (180 $^{\circ}\text{C}$, 10 h). In contrast to the powder of $\text{Ni}_D@NF$ with relatively good crystallinity, obtained nanosheets of $\text{Ni}_{A-S}@NF$ show a c-a coupling structure. Logically, the obvious lattice distortion indicates the desired spatial interruption. Taken together, abundant recycled methanol molecules originated from the adsorbed and surrounding solvent seem to directly induce local amorphization of the original closed-loop crystallization, leading to the c-a hetero-phase structure.

The aforementioned difference suggests that our strategy is effective for c-a coupling on both substrates of CC and NF. To expand the applications of methanol steam-driven reorganization strategy, we turned our attention to the more complicated Ni-Fe precursor solution. By adding $\text{Fe}(\text{NO}_3)_3 \cdot 0.9 \text{H}_2\text{O}$ into the $\text{Ni}(\text{NO}_3)_2$ methanol solution, Fe^{3+} ions were

used to optimize catalytic activity and stability. Without enough nickel nitrate for $\text{NiFe}_{A-S}@CC$, the ellipse structure of iron oxide dominates the major structure (Fig. 1g). Even increasing the ratio of Ni/Fe from 1:2 to 1:1, there are still separated nanosheets and ellipses on CC (Fig. 1h). Interestingly, the surface morphology of $\text{NiFe}_{A-S}@NF$ only shows a high density of uniform nanosheets, with supraaerophobicity and similar shape, vertically grown on the nickel foam (Fig. 1i and Fig. S4). Simultaneously, the elemental mapping confirms the homogeneous distribution of Ni, Fe, N and O (Fig. S5). The increased disorder is evident from the broad peaks observed in its XRD pattern (Fig. 2b and Fig. S1c). It is clear that the (001) diffraction peaks shifts from 12.8° to a lower degree of 12.4° , indicating the successful insertion of Fe^{3+} cations [32]. In comparison with $\text{Fe}_{A-S}@CC$ that contains Fe_2O_3 (PDF#33-0664), no obvious matching characteristic peaks are observed in $\text{NiFe}_{A-S}@NF$. According to the TEM images (Fig. S3b and Fig. 2e), the $\text{NiFe}_{A-S}@NF$ sample shows juxtaposed amorphous and crystalline phases, appearing in adjacent domains. The short lattice fringes with a d -spacing of 0.21 nm correspond to the (102) crystal plane, while most sites show diffuse halo rings in SAED images. So, this design is feasible for more complicated compositions.

By using untreated smooth NFs, we next explored the influence of

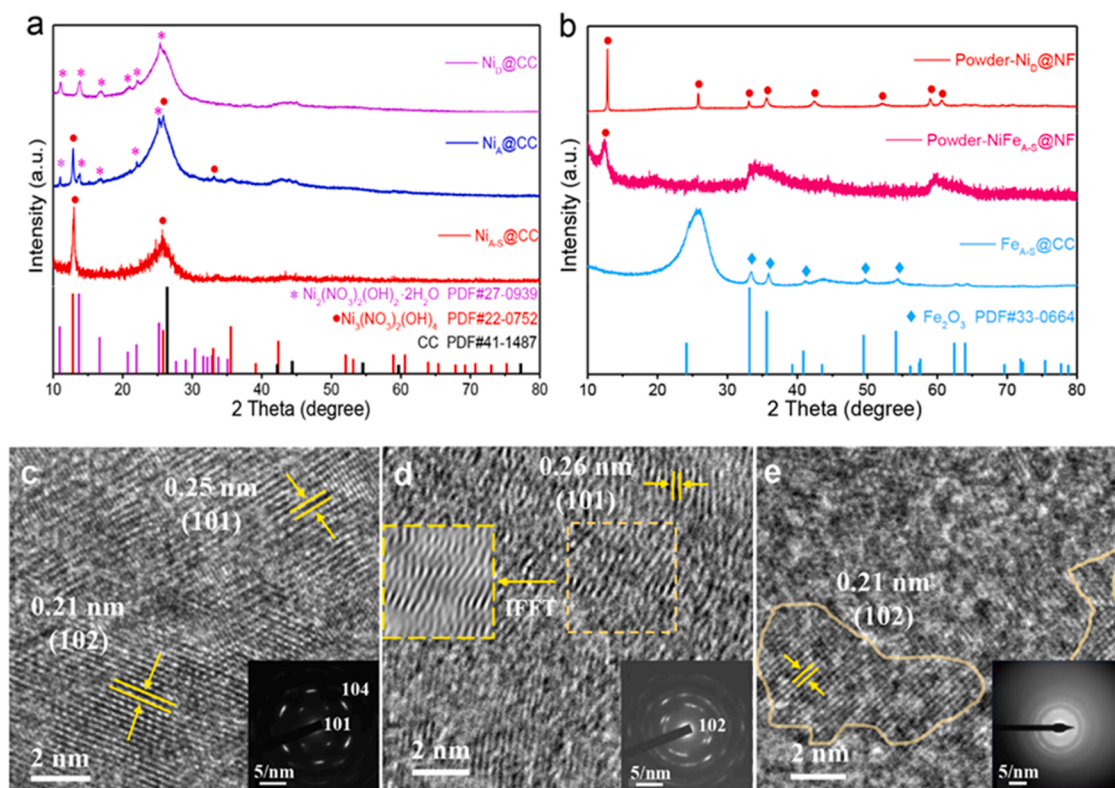


Fig. 2. a-b) XRD patterns of (a) $\text{Ni}_D@CC$, $\text{Ni}_A@CC$, and $\text{Ni}_{A-S}@CC$, in comparison with that of standard $\text{Ni}_2(\text{NO}_3)_2(\text{OH})_2 \cdot 2\text{H}_2\text{O}$ (PDF#27-0939), $\text{Ni}_3(\text{NO}_3)_2(\text{OH})_4$ (PDF#22-0752) and CC (PDF#41-1487) diffractions, (b) Powder- $\text{Ni}_D@NF$, Powder- $\text{NiFe}_{A-S}@NF$ and $\text{Fe}_{A-S}@CC$ in comparison with that of standard Fe_2O_3 diffraction (PDF#33-0664), c-e) TEM images of (c) $\text{Ni}_D@NF$, (d) $\text{Ni}_{A-S}@NF$ and (e) $\text{NiFe}_{A-S}@NF$ (bottom right insets show the corresponding SAED patterns).

Fe^{3+} ions on contact surfaces. The SEM image of $\text{NiFe}_{A-S}@NF$ shows a rough texture over the nickel foam (Fig. S6), while the nanosheets of $\text{Ni}_{A-S}@NF$ are contacting an obviously smoother surface. Simultaneously, even after the ultrasonic treatment, elemental analysis reveals that iron element remains on the rough surface of $\text{NiFe}_{A-S}@NF$. With the help of methanol steam atmosphere and residual water molecules, the bare metallic Ni was oxidized into Ni^{2+} by Fe^{3+} due to its Lewis acidity [33]. The leaching of semi self-sacrificing NF to the NiFe_{A-S} nanosheets is more intuitively evidenced by the corresponding Ni/Fe ratio of nanosheets as shown in Fig. S7. Both ICP and EDX analysis verified the much higher Ni/Fe ratio of about 4:1 compared to the initial reagent ratio of only 1:2. Therefore, during the fabrication of NiFe-LDH , the nickel foam served as both substrate and Ni source, which could enhance its long-term contacting stability. For a semi self-sacrificing preparation method, the size scalability is also one of the core indicators to determine its potential. Considering the uniformity of methanol steam distribution, the preliminary scale-up experiments was unsurprisingly verified by using more precursor solution and bigger Teflon liner. Microstructural characterizations of scaled-up $\text{NiFe}_{A-S}@NF$ (4×5 cm) further confirm the homogeneousness of this steam-driven strategy (Fig. S8).

3.2. Electrocatalytic properties for OER

The self-supporting electrodes of $\text{Ni}_{A-S}@NF$ and $\text{NiFe}_{A-S}@NF$ are taken as research models to interpret the c-a coupling role on promoting OER catalytic performance, as shown in Fig. 3. All data were recorded in a typical three-electrode cell using in-situ formed catalysts as the working electrode. To analyze why the peak current i_p fluctuates during the reversible electron transfer processes, this exploration begins from one certain slow scan rate and without stirring [34]. Within a fixed potential range of 0–0.75 V vs. Hg/HgO, CV was used to provide real-time overpotential values for comparing electrode performances. In

order to avoid the signal overlap between $\text{Ni}^{2+}/\text{Ni}^{3+}$ oxidation peak and OER, polarization curves were recorded from high initial potential to low potential at a scan rate of 5 mV/s. Based on the above settings, collaborative results of the reaction dynamics and the electrochemical surface area can predict how a system will respond to the electrode potential [35,36].

The redox process of $\text{Ni}_{A-S}@NF$ can be easily observed from the CV curves in Fig. 3a. The original anodic peak intensity first increases, followed by emergence of new oxidation waves at more anodic potentials. Some available studies have demonstrated that prolonged cycling can convert $\alpha\text{-Ni}(\text{OH})_2$ to $\beta\text{-Ni}(\text{OH})_2$ [37]. Besides the normal oxidation of Ni^{2+} , three new oxidation peaks are obvious in the LSV curve (Fig. S9). The elevated wave is likely due to the formation of a small amount of Ni^{4+} which is consistent with previously reported works [38]. So, the new oxidation waves could be attributed to $\beta\text{-Ni}(\text{OH})_2$, $\gamma\text{-NiOOH}$ and $\beta\text{-NiOOH}$. After 10 cycles, the intensity of oxidation peaks began to decrease. Subsequently, $\text{Ni}_{A-S}@NF$ electrode shows a gradual decrease in OER activity with increased cycle time. Despite the presence of Ni^{4+} , the formation of $\beta\text{-Ni}(\text{OH})_2/\beta\text{-NiOOH}$ does not show an intrinsically higher OER activity than $\alpha\text{-Ni}(\text{OH})_2/\gamma\text{-NiOOH}$. Throughout the continuous CV scanning, the decreasing tendency is further evidenced by LSV curves (Fig. 3b) and EIS curves (Fig. 3c). The chronopotentiometric test was carried out at a small constant current density of 10 mA cm^{-2} . Unsurprisingly, only after 20 h, the durability curve in Fig. 3d shows that the real-time overpotential exhibits an obvious increase of 70 mV. Here, the main cause of this observed weakening can due to the serious peeling of catalytic active species from NF substrates during the oxygen evolution process.

In general, the coprecipitated Fe^{3+} usually triggers a slight fluctuation during continuous CV cycles even in purified electrolyte [39,40]. Interestingly, compared with $\text{Ni}_3(\text{NO}_3)_2(\text{OH})_4$ of $\text{Ni}_{A-S}@NF$, the $\text{NiFe}_{A-S}@NF$ electrode exhibits an enhanced activation process under the same condition (Fig. 3e-i). Throughout this continuous CV scanning, the

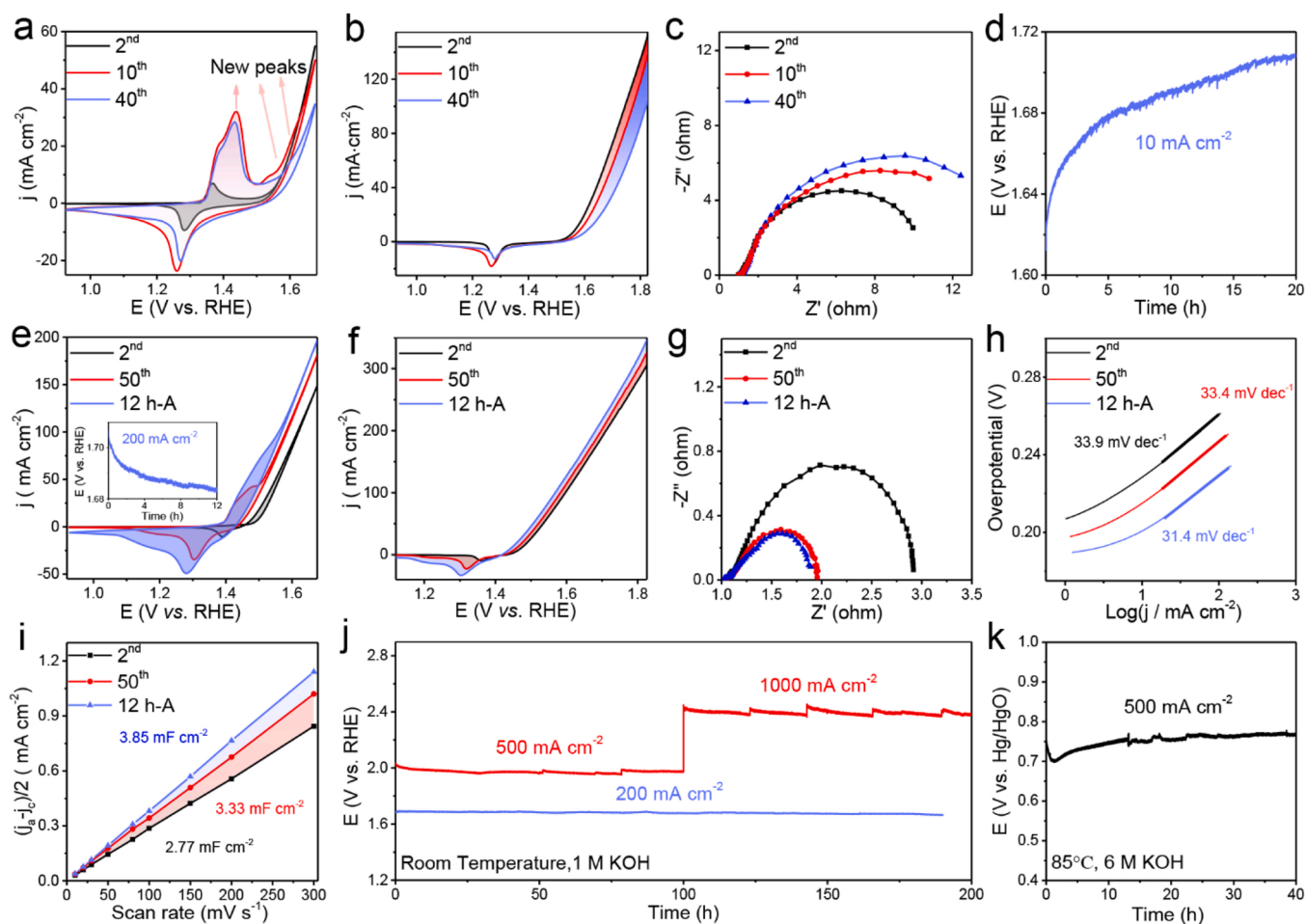


Fig. 3. a-d) Ni_{A-S}@NF electrocatalytic measurements including (a) CV curves, (b) LSV curves, (c) Nyquist plots and (d) Durability test (10 mA cm⁻²), e-k) NiFe_{A-S}@NF electrocatalytic measurements including (e) CV curves, inset shows time-dependent potential curve at 200 mA cm⁻² for 12 h (labeled as 12 h-A) (f) LSV curves, (g) Nyquist plots, (h) Tafel slopes, (i) C_{dl} measurements, (j) Long-term durability tests at large current densities of 200, 500, and 1000 mA cm⁻² and (k) under industry operating conditions.

improvement was observed to be significant initially and then gradually turned to be moderate. To be more precise, the peak current increased and position gradually shifted to the cathodic side along the CV cycles. After continuous 12-h electrochemical activation at 200 mA cm⁻², the peak intensity of activated sample (12 h-A) became stronger, and position slightly moved to the anodic side. Meanwhile, the presence of Fe³⁺ prevented the transformation of α -Ni(OH)₂ into β -Ni(OH)₂ [41]. As presented in Fig. 3f, LSV curves show that the initial catalyst has a poor OER activity. By contrast, 12 h-A has an impressively low overpotential of only 205 mV to reach a current density of 10 mA cm⁻². Investigated by Nyquist and Tafel plots, it is obvious that repeated CV scans promoted OER kinetics during this activation process. Comparing with 2nd and 50th-cycled samples (Fig. 3g), 12 h-A displays a much lower charge transfer resistance, indicating that the activation process can markedly facilitate charge transfer. Considering aforementioned CV curves, Tafel slopes are directly calculated from LSV curves. A small Tafel slope is obtained for the pristine NiFe_{A-S}@NF after being activated (Fig. 3h). Overall, even for the high ratio of Fe³⁺ in precursor, there is only an integral NiFe-LDH after ultrasonic cleaning [42]. Following, the analysis of enhanced peak values is carried out using the Randles-Sevcik equation. As deduced from the equation, the exposed active area of this catalyst should change accordingly. The electrochemical active surface area (ECSA) was estimated based on the double-layer capacitances (C_{dl}) of electrocatalyst (Fig. 3i) from the corresponding CV profiles measured in the non-Faradaic potential ranges at various scan rates (Fig. S10). 12 h-A has a C_{dl} value of 3.81 mF cm⁻², which is larger than that of 50th

(3.35 mF cm⁻²) and 2nd (2.77 mF cm⁻²). The high C_{dl} value of activated NiFe_{A-S}@NF demonstrates clear advantages of the c-a structure which can provide more accessible catalytic sites. To carefully verify the process of NiFe_{A-S}@NF being studied, another counter electrode of graphite rod was selected to repeat the electrochemical activation and measurements. The undifferentiated reaction process (Fig. S11) allows us to rule out the effect of counter electrodes. Likewise, the enlarged NiFe_{A-S}@NF (4 × 5 cm) also displays similar electrochemical activation process (Fig. S12). As a result, the enhanced redox peak value can be attributed to the increasing electrochemical surface area, in line with the boosted OER catalytic activity displayed in the polarization curves.

As a promising design, the prepared catalyst should energetically survive high current density under high temperature and electrolyte concentrations (Fig. 3j). It has been generally accepted that the layered structure makes bulk NiFe-LDHs intrinsically not stable in OER [43,44]. During OER, the slow diffusion of proton acceptors within the interlayers causes dissolution of NiFe-LDHs with time. Herein, the activated NiFe_{A-S}@NF catalyst shows a favorable operating stability, providing a stable 200 mA cm⁻² current density for a period of 200 h without obvious potential increase. It is worth noting that the c-a nanosheets are still tightly anchored on NF as before, indicating the high morphology stability (Fig. S13). Furthermore, according to TEM images and EDX spectrum (Fig. S14), Fe, Ni and O elements are homogeneously distributed after the durability test. As for the long-term durability test conducted at 500 mA cm⁻² for 100 h immediately followed by 1000 mA cm⁻² for 100 h, the real-time potential presents no obvious

increase. LSV curves collected before and after the stability testing only show a slight shift, confirming the superior stability of NiFe_{A-S}@NF for the large current OER (Fig. S15). Even under the close to industrial conditions of 85 °C and 6 M KOH, NiFe_{A-S}@NF still undergoes the test of structural stability. There is only less than 10% increase of the potential while holding the high current density of 500 mA cm⁻² for 40 h (Fig. 3k), further supporting the high operational stability. Thus, the activated c-a coupling structure can survive large current density and high temperature over a long period of time, beneficial for future industrial applications. Compared to recently reported OER catalysts with c-a or c/a structures, NiFe_{A-S}@NF presents the significant stability advantage (Table S1). This homogenous c-a structure is one of the highest potential design, especially for large current densities.

3.3. Insights into the activation process of NiFe_{A-S}@NF

To understand the origin of high catalytic activity, the structural transformation of fresh NiFe_{A-S}@NF was investigated by operando Raman. Before any electrochemical activation, there are two rather low and broad bands centered at about 525 cm⁻¹ and 702 cm⁻¹, which are assigned to Ni^{II}-OH and Ni^{II}O-H bands (Fig. 4a) [37]. Signals of surface structure conversion become clear after the oxidation peak. The appearance of two new Raman bands at 474 cm⁻¹ and 554 cm⁻¹, ascribed to the E_g Ni^{III}-O bending vibration mode and A_{1g} Ni^{III}-O stretching vibration, suggests the formation of NiOOH phase [45]. After starting of the surface evolution, the reversible Ni²⁺ transformation exhibits obvious electrochemical dependence. When the potential was reduced back to 0.93 V vs. RHE, two low and broad peaks of NiOOH still existed (Fig. S16). This suggests most of the formed NiOOH did not transform back to Ni(OH)₂ species [46]. As shown in Fig. 4b, relative intensities of the above two bands (I₄₇₄/I₅₅₄) show obvious enhanced tendency along the multipotential I-t measurement (Fig. S17). It is noteworthy that

operando Raman characterization method often fails to identify the formation of FeOOH species [47,48]. Herein, starting from the first polarization, our studies did not observe well-defined Raman peak of Fe³⁺ species (such as Fe₂O₃ or FeOOH) likely due to the amorphous phase and the relatively lower Fe content on the surface region.

To gain in-depth insight into the intrinsic activity (without NF) during the OER process, we next tracked the sorption-desorption behavior using EQCM-D, which measures fluctuations of both resonance frequency (f) and energy dissipation (D) [49]. In this quantification model, fluctuations of Δf and ΔD are linear functions with Sauerbrey mass (M) and energy losses. Since D-values reach almost steady state after the injection of KOH (Fig. S18), assuming a rigid film, the Sauerbrey equation can be used for correlating oscillation frequency with the NiFe_{A-S} sample mass change. From the inserted CV curves, the current intensity reflects an obvious upward gain (Fig. 4c). Along with the periodic sorption-desorption change, the time profile of Sauerbrey mass indicates an overall gradually increasing trend. Given the real-time information of this surface-sensitive technique, the fluctuation can directly relate to the activation process of NiFe_{A-S} powder. After the electrochemical activation, the second peak position of inset CVs agrees well with the third oxidation peak of Ni_{A-S}@NF (Fig. S9). Here, different from above-mentioned NiFe_{A-S}@NF curves (Fig. 4e and f), the presence of Ni⁴⁺ can be clearly observed on the gold sensor. As verified from monometallic nickel hydroxy-nitrate to bimetallic NiFe-LDH, we reasoned that steam-driven c-a coupling could help elevate a small fraction of Ni atoms to the higher valence state (Ni⁴⁺) during OER, which provides an effective avenue to enhance the OER catalytic activity of NiFe_{A-S}@NF. Meantime, ΔD/n also displays an increasing trend (Fig. S19), suggesting that the surface became softer. This tendency may be explained by the modified active surface, which has a softer structure and more readily accessible active sites. Therefore, the activation process gradually optimizes the structure of active centers, making them

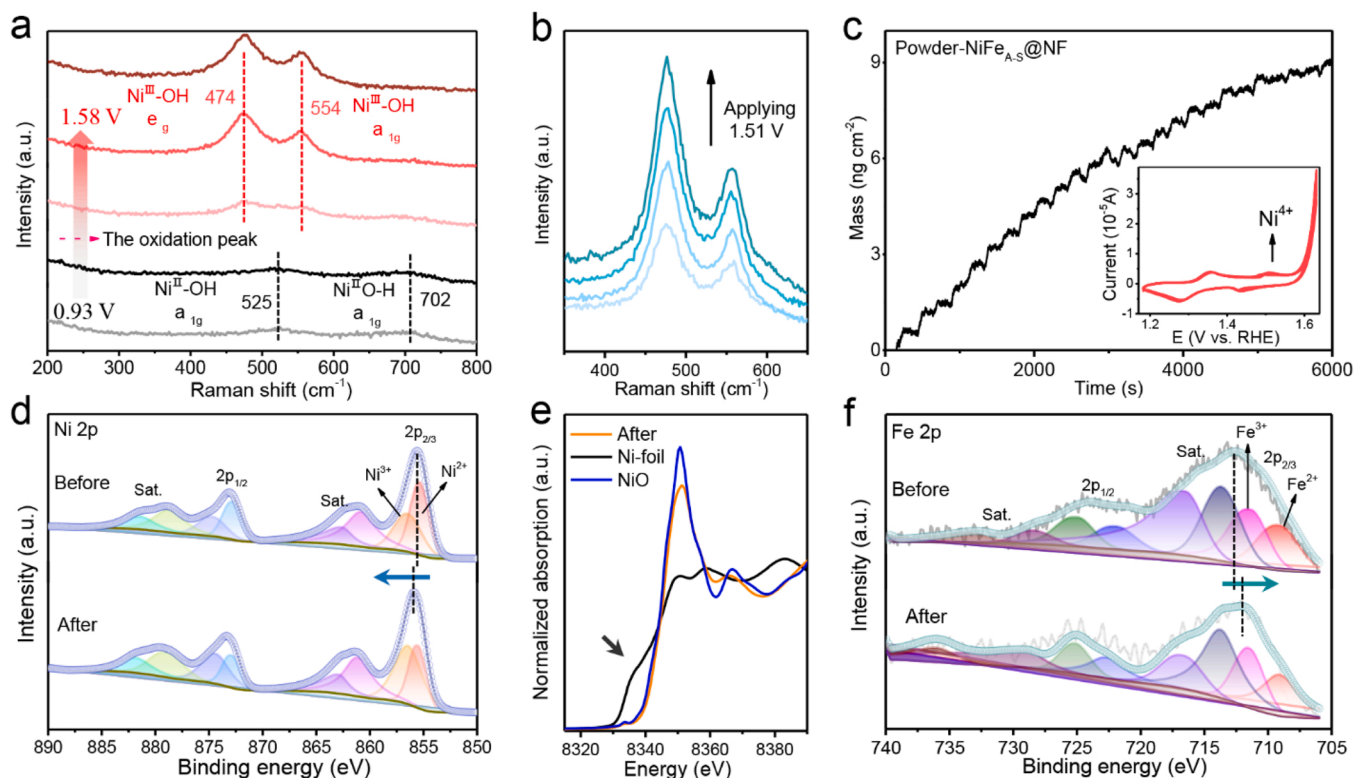


Fig. 4. Surface electronic characterizations of NiFe_{A-S}@NF. (a) Operando Raman spectra collected at different potentials (0.93–1.58 V vs. RHE), (b) The corresponding operando Raman spectra during chronoamperometry measurement, (c) Mass vs time showing the periodic fluctuations during CV cycles, inset is the corresponding CVs, (d) Ni 2p XPS spectra before and after activation process, (e) XANES spectra Ni K-edge after activation process, (f) Fe 2p XPS spectra before and after activation process.

much more adaptive and suitable for adsorbing reactant species.

We then used X-ray photoelectron spectroscopy (XPS) to identify the chemical composition and oxidation state of in-situ formed NiFe-LDH (Fig. S20). The synergistic electronic effect was investigated by collecting NiFe_{A-S} powder samples which were peeled off from the NF substrate before and after activation process. As shown in the fine-scanning Ni 2p spectrum (Fig. 4d), two spin-orbit doublets of Ni 2p_{3/2} (855.4 eV), Ni 2p_{1/2} (872.9 eV) and satellites (860.8 eV and 879.8 eV, abbreviated as “sat.”) can be indexed to Ni²⁺, while another pair of peaks (856.6 and 874.8 eV) and satellites (862.8 eV and 881.5 eV) are assigned to Ni³⁺. More importantly, the Ni 2p_{3/2} peak of post-OER Ni-Fe (oxy)hydroxides obviously shifts to binding energy of 855.6 eV, suggesting that partial electrons are transferred. In addition, the ratio of Ni³⁺ 2p_{3/2}/Ni²⁺ 2p_{3/2} is significantly larger than that of pristine powder of NiFe_{A-S}@NF, suggesting the enriched superficial oxyhydroxide transformation of metal sites during electrochemical activation. Above results reveal that the enriched Ni³⁺ species of activated NiFe-LDH is responsible for OER catalytic activity enhancement. As depicted in Fig. 4e, the Ni K-edge indicates a higher average valence state of Ni atom, agreeing well with Ni 2p XPS spectra [50]. Similarly, the binding energies of two peaks at approximately 709 eV and 711 eV correspond to Fe²⁺ and Fe³⁺ (Fig. 4f), respectively [51]. Correspondingly, the ratio of Fe³⁺ 2p_{3/2}/Fe²⁺ 2p_{3/2} decreased from 1.22 to 1.02, which could be ascribed to efficient electron transfer from Ni to Fe, likely strengthened by the coordinated oxygen between Ni and Fe [52].

The preceding analysis provides compelling evidence that the encouraging catalytic activity of optimal NiFe-LDH benefits from our unique design, which are: (i) the abundant c-a coupling phases provide a desirable electronic structure including the high valence Ni⁴⁺; (ii) the addition of Fe³⁺ not only stabilizes the microstructure of Ni₃(NO₃)₂(OH)₄ but also promotes the reaction kinetics; (iii) The semi self-sacrificing NF leads to the strong adhesion of bimetallic NiFe-LDH nanosheets which is beneficial for their long-term mechanical stability during the durability test.

4. Conclusion

A novel methanol steam-driven technique was developed to overcome the limitations of asynchronous growth and first exemplified for the fabrication of Ni-hydroxy-nitrates on CC and NF with controlled phase distribution. The formation mechanism of the desirable juxtaposed c-a structure within uniform chemical composition was systematically discussed. Local changes in water content, combined with the obvious modulation effects of methanol steam, are offered as plausible explanations for different chemical compositions and growth tendencies. By simply adding Fe³⁺ ions to the Ni precursor solution, this method was successfully extended to NiFe-LDH nanosheets with excellent OER activity and remarkable durability at large current densities. The complementary analysis of electrochemical measurements, operando Raman, EQCM-D, XPS and XANES studies further reveals that the stable coupled c-a phases not only facilitate charge transfer but also increase the effective electrochemical surface area. With the benefits of simple synthesis and facile phase transformation, our methanol steam-driven strategy developed here represents a significant step forward in designing better and cheaper electrocatalysts for industrial applications.

CRedit authorship contribution statement

Jinqiang Gao: Conceptualization, Investigation, Writing – original draft. **Chen Qiu:** Validation. **Min Ju:** Formal analysis. **Simeng Li:** Data curation. **Rongxing Yu:** Investigation. **Hongzhi Liu:** Investigation. **Mingyu Hu:** Writing – review & editing. **Jun Yu:** Funding acquisition. **Mei Hong:** Project administration, Writing – review & editing, Validation, Funding acquisition. **Shihe Yang:** Supervision, Writing – review & editing. **Validation, Funding acquisition.**

Declaration of Competing Interest

The authors declare that they have no known competing financial interests or personal relationships that could have appeared to influence the work reported in this paper.

Data Availability

Data will be made available on request.

Acknowledgments

This work was supported by the National Natural Science Foundation of China (21972006), the Shenzhen Science and Technology Program (JCYJ20200109140421071, JSGG20211029095546003, KCXFZ2020 1221173604012), and Shenzhen Peacock Plan (KQTD20160530 15544057).

Appendix A. Supporting information

Supplementary data associated with this article can be found in the online version at doi:10.1016/j.apcatb.2022.122165.

References

- [1] L.C. Seitz, C.F. Dickens, K. Nishio, Y. Hikita, J. Montoya, A. Doyle, C. Kirk, A. Vojvodic, H.Y. Hwang, J.K. Norskov, T.F. Jaramillo, A highly active and stable IrO_x/SrIrO₃ catalyst for the oxygen evolution reaction, *Science* 353 (2016) 1011–1014, <https://doi.org/10.1126/science.aaf5050>.
- [2] H. Han, Y. Qiu, H. Zhang, T. Bi, Q. Yang, M. Liu, J. Zhou, X. Ji, Lattice-disorder layer generation from liquid processing at room temperature with boosted nanointerface exposure toward water splitting, *Sustain. Energy Fuels* 6 (2022) 3008–3013, <https://doi.org/10.1039/D2SE00474G>.
- [3] Y. Li, Y. Wu, M. Yuan, H. Hao, Z. Lv, L. Xu, B. Wei, Operando spectroscopies unveil interfacial FeOOH induced highly reactive β-Ni(Fe)OOH for efficient oxygen evolution, *Appl. Catal. B Environ.* 318 (2022), 121825, <https://doi.org/10.1016/j.apcatb.2022.121825>.
- [4] A. Saad, D.Q. Liu, Y.C. Wu, Z.Q. Song, Y. Li, T. Najam, K. Zong, P. Tsiakaras, X. K. Cai, Ag nanoparticles modified crumpled borophene supported Co₃O₄ catalyst showing superior oxygen evolution reaction (OER) performance, *Appl. Catal. B Environ.* 298 (2021), 120529, <https://doi.org/10.1016/j.apcatb.2021.120529>.
- [5] L. Lv, Z. Yang, K. Chen, C. Wang, Y. Xiong, 2D layered double hydroxides for oxygen evolution reaction: from fundamental design to application, *Adv. Energy Mater.* 9 (2019) 1803358, <https://doi.org/10.1002/aenm.201803358>.
- [6] J. Kang, X. Qiu, Q. Hu, J. Zhong, X. Gao, R. Huang, C. Wan, L.-M. Liu, X. Duan, L. Guo, Valence oscillation and dynamic active sites in monolayer NiCo hydroxides for water oxidation, *Nat. Catal.* 4 (2021) 1050–1058, <https://doi.org/10.1038/s41929-021-00715-w>.
- [7] J. Wang, Y. Gao, H. Kong, J. Kim, S. Choi, F. Ciucci, Y. Hao, S. Yang, Z. Shao, J. Lim, Non-precious-metal catalysts for alkaline water electrolysis: operando characterizations, theoretical calculations, and recent advances, *Chem. Soc. Rev.* 49 (2020) 9154–9196, <https://doi.org/10.1039/d0cs00575d>.
- [8] J. Wang, S.-J. Kim, J. Liu, Y. Gao, S. Choi, J. Han, H. Shin, S. Jo, J. Kim, F. Ciucci, H. Kim, Q. Li, W. Yang, X. Long, S. Yang, S.-P. Cho, K.H. Chae, M.G. Kim, H. Kim, J. Lim, Redirecting dynamic surface restructuring of a layered transition metal oxide catalyst for superior water oxidation, *Nat. Catal.* 4 (2021) 212–222, <https://doi.org/10.1038/s41929-021-00578-1>.
- [9] C. Li, L. Zhang, J. Chen, X. Li, J. Sun, J. Zhu, X. Wang, Y. Fu, Recent development and applications of electrical conductive MOFs, *Nanoscale* 13 (2021) 485–509, <https://doi.org/10.1039/d0nr06396g>.
- [10] F. Gao, J. He, H. Wang, J. Lin, R. Chen, K. Yi, F. Huang, Z. Lin, M. Wang, Te-mediated electro-driven oxygen evolution reaction, *Nano Res. Energy* 1 (2022), e9120029, <https://doi.org/10.26599/NRE.2022.9120029>.
- [11] C. Ye, L. Zhang, L. Yue, B. Deng, Y. Cao, Q. Liu, Y. Luo, S. Lu, B. Zheng, X. Sun, A NiCo LDH nanosheet array on graphite felt: an efficient 3D electrocatalyst for the oxygen evolution reaction in alkaline media, *Inorg. Chem. Front.* 8 (2021) 3162–3166, <https://doi.org/10.1039/d1qi00428j>.
- [12] L. Zhang, J. Wang, P. Liu, J. Liang, Y. Luo, G. Cui, B. Tang, Q. Liu, X. Yan, H. Hao, M. Liu, R. Gao, X. Sun, Ni(OH)₂ nanoparticles encapsulated in conductive nanowire array for high-performance alkaline seawater oxidation, *Nano Res.* 15 (2022) 6084–6090, <https://doi.org/10.1007/s12274-022-4391-6>.
- [13] Y. Qiu, J. Zhou, Z. Liu, X. Zhang, H. Han, X. Ji, J. Liu, Solar-driven photoelectron injection effect on MgCo₂O₄@WO₃ core-shell heterostructure for efficient overall water splitting, *Appl. Surf. Sci.* 578 (2022), 152049, <https://doi.org/10.1016/j.apsusc.2021.152049>.
- [14] Y. Cao, T. Wang, X. Li, L. Zhang, Y. Luo, F. Zhang, A.M. Asiri, J. Hu, Q. Liu, X. Sun, A hierarchical CuO@NiCo layered double hydroxide core-shell nanoarray as an

- efficient electrocatalyst for the oxygen evolution reaction, *Inorg. Chem. Front.* 8 (2021) 3049–3054, <https://doi.org/10.1039/d1qi00124h>.
- [15] Y. Qiu, Z. Liu, X. Zhang, A. Sun, X. Ji, J. Liu, Controllable atom implantation for achieving Coulomb-force unbalance toward lattice distortion and vacancy construction for accelerated water splitting, *J. Colloid Interface Sci.* 610 (2022) 194–201, <https://doi.org/10.1016/j.jcis.2021.12.029>.
- [16] S. Zhao, C. Tan, C.-T. He, P. An, F. Xie, S. Jiang, Y. Zhu, K.-H. Wu, B. Zhang, H. Li, J. Zhang, Y. Chen, S. Liu, J. Dong, Z. Tang, Structural transformation of highly active metal-organic framework electrocatalysts during the oxygen evolution reaction, *Nat. Energy* 5 (2020) 881–890, <https://doi.org/10.1038/s41560-020-00709-1>.
- [17] S.L. Zhang, B.Y. Guan, X.F. Lu, S. Xi, Y. Du, X.W.D. Lou, Metal atom-doped Co₃O₄ hierarchical nanoplates for electrocatalytic oxygen evolution, *Adv. Mater.* 32 (2020) 2002235, <https://doi.org/10.1002/adma.202002235>.
- [18] S. Du, Z. Ren, X. Wang, J. Wu, H. Meng, H. Fu, Controlled atmosphere corrosion engineering toward inhomogeneous NiFe-LDH for energetic oxygen evolution, *ACS Nano* 16 (2022) 7794–7803, <https://doi.org/10.1021/acsnano.2c00332>.
- [19] B.H.R. Suryanto, Y. Wang, R.K. Hocking, W. Adamson, C. Zhao, Overall electrochemical splitting of water at the heterogeneous interface of nickel and iron oxide, *Nat. Commun.* 10 (2019) 5599, <https://doi.org/10.1038/s41467-019-13415-8>.
- [20] C. Spori, L.J. Falling, M. Kroschel, C. Brand, A. Bonakdarpour, S. Kuhl, D. Berger, M. Glicke, T.E. Jones, D.P. Wilkinson, P. Strasser, Molecular analysis of the unusual stability of an IrNbOx catalyst for the electrochemical water oxidation to molecular oxygen (OER), *ACS Appl. Mater. Interfaces* 13 (2021) 3748–3761, <https://doi.org/10.1021/acsaami.0c12609>.
- [21] Z. Chen, M. Ju, M. Sun, L. Jin, R. Cai, Z. Wang, L. Dong, L. Peng, X. Long, B. Huang, S. Yang, T.M. LDH Meets Birnessite, A ²D-²D, Hybrid catalyst with long-term stability for water oxidation at industrial operating conditions, *Angew. Chem. Int. Ed. Engl.* 60 (2021) 9699–9705, <https://doi.org/10.1002/anie.202016064>.
- [22] S. Li, X. Yang, S. Yang, Q. Gao, S. Zhang, X. Yu, Y. Fang, S. Yang, X. Cai, An amorphous trimetallic (Ni–Co–Fe) hydroxide-sheathed 3D bifunctional electrode for superior oxygen evolution and high-performance cable-type flexible zinc–air batteries, *J. Mater. Chem. A* 8 (2020) 5601–5611, <https://doi.org/10.1039/d0ta00888e>.
- [23] G. Wan, J.W. Freeland, J. Kloppenburg, G. Petretto, J.N. Nelson, D.Y. Kuo, C. J. Sun, J. Wen, J.T. Diulus, G.S. Herman, Y. Dong, R. Kou, J. Sun, S. Chen, K. M. Shen, D.G. Schlom, G.M. Rignanes, G. Hautier, D.D. Fong, Z. Feng, H. Zhou, J. Suntivich, Amorphization mechanism of SrIrO₃ electrocatalyst: how oxygen redox initiates ionic diffusion and structural reorganization, *Sci. Adv.* 7 (2021) eabc7323, <https://doi.org/10.1126/sciadv.abc7323>.
- [24] X. Zhang, Z. Luo, P. Yu, Y. Cai, Y. Du, D. Wu, S. Gao, C. Tan, Z. Li, M. Ren, T. Osipowicz, S. Chen, Z. Jiang, J. Li, Y. Huang, J. Yang, Y. Chen, C.Y. Ang, Y. Zhao, P. Wang, L. Song, X. Wu, Z. Liu, A. Borgna, H. Zhang, Lithiation-induced amorphization of Pd₃P₂S₈ for highly efficient hydrogen evolution, *Nat. Catal.* 1 (2018) 460–468, <https://doi.org/10.1038/s41929-018-0072-y>.
- [25] C. Guo, Y. Shi, S. Lu, Y. Yu, B. Zhang, Amorphous nanomaterials in electrocatalytic water splitting, *Chin. J. Catal.* 42 (2021) 1287–1296, [https://doi.org/10.1016/s1872-2067\(20\)63740-8](https://doi.org/10.1016/s1872-2067(20)63740-8).
- [26] G. Chen, Y. Zhu, H.M. Chen, Z. Hu, S.F. Hung, N. Ma, J. Dai, H.J. Lin, C.T. Chen, W. Zhou, Z. Shao, An amorphous nickel-iron-based electrocatalyst with unusual local structures for ultrafast oxygen evolution reaction, *Adv. Mater.* 31 (2019) 1900883, <https://doi.org/10.1002/adma.201900883>.
- [27] S. Shen, Z. Wang, Z. Lin, K. Song, Q. Zhang, F. Meng, L. Gu, W. Zhong, Crystalline-amorphous interfaces coupling of CoSe₂/CoP with optimized d-Band center and boosted electrocatalytic hydrogen evolution, *Adv. Mater.* 34 (2022) 2110631, <https://doi.org/10.1002/adma.202110631>.
- [28] M. Kuang, J. Zhang, D. Liu, H. Tan, K.N. Dinh, L. Yang, H. Ren, W. Huang, W. Fang, J. Yao, X. Hao, J. Xu, C. Liu, L. Song, B. Liu, Q. Yan, Amorphous/crystalline heterostructured cobalt-vanadium-iron (Oxy)hydroxides for highly efficient oxygen evolution reaction, *Adv. Energy Mater.* 10 (2020) 2002215, <https://doi.org/10.1002/aenm.202002215>.
- [29] D. Li, Y. Qin, J. Liu, H. Zhao, Z. Sun, G. Chen, D.Y. Wu, Y. Su, S. Ding, C. Xiao, Dense crystalline–amorphous interfacial sites for enhanced electrocatalytic oxygen evolution, *Adv. Funct. Mater.* 32 (2021) 2107056, <https://doi.org/10.1002/adfm.202107056>.
- [30] C. Liang, P. Zou, A. Nairan, Y. Zhang, J. Liu, K. Liu, S. Hu, F. Kang, H.J. Fan, C. Yang, Exceptional performance of hierarchical Ni–Fe oxyhydroxide@NiFe alloy nanowire array electrocatalysts for large current density water splitting, *Energy Environ. Sci.* 13 (2020) 86–95, <https://doi.org/10.1039/c9ee02388g>.
- [31] H. Han, H. Choi, S. Mhin, Y.-R. Hong, K.M. Kim, J. Kwon, G. Ali, K.Y. Chung, M. Je, H.N. Uhm, D.-H. Lim, K. Davey, S.-Z. Qiao, U. Paik, T. Song, Advantageous crystalline–amorphous phase boundary for enhanced electrochemical water oxidation, *Energy Environ. Sci.* 12 (2019) 2443–2454, <https://doi.org/10.1039/c9ee00950g>.
- [32] J. Zhao, J.J. Zhang, Z.Y. Li, X.H. Bu, Recent progress on NiFe-based electrocatalysts for the oxygen evolution reaction, *Small* 16 (2020) 2003916, <https://doi.org/10.1002/smll.202003916>.
- [33] X. Li, C. Liu, Z. Fang, L. Xu, C. Lu, W. Hou, Ultrafast room-temperature synthesis of self-supported nife-layered double hydroxide as large-current-density oxygen evolution electrocatalyst, *Small* 18 (2022) 2104354, <https://doi.org/10.1002/smll.202104354>.
- [34] N. Elgrishi, K.J. Rountree, B.D. McCarthy, E.S. Rountree, T.T. Eisenhart, J. L. Dempsey, A practical Beginner's guide to cyclic voltammetry, *J. Chem. Educ.* 95 (2017) 197–206, <https://doi.org/10.1021/acs.jchemed.7b00361>.
- [35] D. Tyndall, S. Jaskaniec, B. Shortall, A. Roy, L. Gannon, K. O'Neill, M.P. Browne, J. Coelho, C. McGuinness, G.S. Duesberg, V. Nicolosi, Postsynthetic treatment of nickel–iron layered double hydroxides for the optimum catalysis of the oxygen evolution reaction, *npj 2D Mater. Appl.* 5 (2021) 73, <https://doi.org/10.1038/s41699-021-00249-6>.
- [36] M.B. Stevens, L.J. Enman, A.S. Batchellor, M.R. Cosby, A.E. Vise, C.D.M. Trang, S. W. Boettcher, Measurement techniques for the study of thin film heterogeneous water oxidation electrocatalysts, *Chem. Mater.* 29 (2016) 120–140, <https://doi.org/10.1021/acs.chemmater.6b02796>.
- [37] L. Peng, N. Yang, Y. Yang, Q. Wang, X. Xie, D. Sun-Waterhouse, L. Shang, T. Zhang, G.I.N. Waterhouse, Atomic cation-vacancy engineering of NiFe-layered double hydroxides for improved activity and stability towards the oxygen evolution reaction, *Angew. Chem. Int. Ed. Engl.* 60 (2021) 24612–24619, <https://doi.org/10.1002/anie.202109938>.
- [38] L. Trotochaud, S.L. Young, J.K. Ranney, S.W. Boettcher, Nickel-iron oxyhydroxide oxygen-evolution electrocatalysts: the role of intentional and incidental iron incorporation, *J. Am. Chem. Soc.* 136 (2014) 6744–6753, <https://doi.org/10.1021/ja502379c>.
- [39] Z. Kuang, S. Liu, X. Li, M. Wang, X. Ren, J. Ding, R. Ge, W. Zhou, A.I. Rykov, M. T. Sougrati, T.C. Weng, R. Alonso-Mori, R.C. Davis, J.R. Bargar, J.K. Norskov, A. Nilsson, A.T. Bell, Identification of highly active Fe sites in (Ni,Fe)OOH for electrocatalytic water splitting, *J. Am. Chem. Soc.* 137 (2015) 1305–1313, <https://doi.org/10.1021/ja511559d>.
- [40] W. Zhang, D. Li, L. Zhang, X. She, D. Yang, NiFe-based nanostructures on nickel foam as highly efficient electrocatalysts for oxygen and hydrogen evolution reactions, *J. Energy Chem.* 39 (2019) 39–53, <https://doi.org/10.1016/j.jechem.2019.01.017>.
- [41] D. Friebe, M.W. Louie, M. Bajdich, K.E. Sanwald, Y. Cai, A.M. Wise, M.J. Cheng, D. Sokaras, T.C. Weng, R. Alonso-Mori, R.C. Davis, J.R. Bargar, J.K. Norskov, A. Nilsson, A.T. Bell, Identification of highly active Fe sites in (Ni,Fe)OOH for electrocatalytic water splitting, *J. Am. Chem. Soc.* 137 (2015) 1305–1313, <https://doi.org/10.1021/ja511559d>.
- [42] C.F. Li, J.W. Zhao, L.J. Xie, J.Q. Wu, Q. Ren, Y. Wang, G.R. Li, Surface-adsorbed carboxylate ligands on layered double hydroxides/metal-organic frameworks promote the electrocatalytic oxygen evolution reaction, *Angew. Chem. Int. Ed. Engl.* 60 (2021) 18129–18137, <https://doi.org/10.1002/anie.202104148>.
- [43] R. Chen, S.F. Hung, D. Zhou, J. Gao, C. Yang, H. Tao, H.B. Yang, L. Zhang, L. Zhang, Q. Xiong, H.M. Chen, B. Liu, Layered structure causes bulk NiFe layered double hydroxide unstable in alkaline oxygen evolution reaction, *Adv. Mater.* 31 (2019) 1903909, <https://doi.org/10.1002/adma.201903909>.
- [44] L. Zhang, J. Liang, L. Yue, K. Dong, J. Li, D. Zhao, Z. Li, S. Sun, Y. Luo, Q. Liu, G. Cui, A. Ali Alshehri, X. Guo, X. Sun, Benzoate anions-intercalated NiFe-layered double hydroxide nanosheet array with enhanced stability for electrochemical seawater oxidation, *Nano Res. Energy* 1 (2022), e9120028, <https://doi.org/10.26599/NRE.2022.9120028>.
- [45] J. Huang, Y. Li, Y. Zhang, G. Rao, C. Wu, Y. Hu, X. Wang, R. Lu, Y. Li, J. Xiong, Identification of key reversible intermediates in self-reconstructed nickel-based hybrid electrocatalysts for oxygen evolution, *Angew. Chem. Int. Ed. Engl.* 58 (2019) 17458–17464, <https://doi.org/10.1002/anie.201910716>.
- [46] S. Zuo, Z.P. Wu, H. Zhang, X.W. Lou, Operando monitoring and deciphering the structural evolution in oxygen evolution electrocatalysis, *Adv. Energy Mater.* 12 (2022) 2103383, <https://doi.org/10.1002/aenm.202103383>.
- [47] M.W. Louie, A.T. Bell, An investigation of thin-film Ni-Fe oxide catalysts for the electrochemical evolution of oxygen, *J. Am. Chem. Soc.* 135 (2013) 12329–12337, <https://doi.org/10.1021/ja405351s>.
- [48] L. Gao, X. Cui, Z. Wang, C.D. Sewell, Z. Li, S. Liang, M. Zhang, J. Li, Y. Hu, Z. Lin, Operando unraveling photothermal-promoted dynamic active-sites generation in NiFe₂O₄ for markedly enhanced oxygen evolution, *e2023421118*, *Proc. Natl. Acad. Sci. USA* 118 (2021), <https://doi.org/10.1073/pnas.2023421118>.
- [49] M. Ju, R. Cai, J. Ren, J. Chen, L. Qi, X. Long, S. Yang, Conductive polymer intercalation tunes charge transfer and sorption-desorption properties of LDH enabling efficient alkaline water oxidation, *ACS Appl. Mater. Interfaces* 13 (2021) 37063–37070, <https://doi.org/10.1021/acsaami.1c08429>.
- [50] J. Yu, J. Wang, X. Long, L. Chen, Q. Cao, J. Wang, C. Qiu, J. Lim, S. Yang, Formation of FeOOH nanosheets induces substitutional doping of CeO_{2-x} with high-valence Ni for efficient water oxidation, *Adv. Energy Mater.* 11 (2020) 2002731, <https://doi.org/10.1002/aenm.202002731>.
- [51] D. Shu, H. Liu, T. Chen, D. Chen, X. Zou, C. Wang, M. Li, H. Wang, The positive effect of siderite-derived α-Fe₂O₃ during coating on the NO behavior in the presence of NH₃, *Environ. Sci. Pollut. Res.* 27 (2020) 12376–12385, <https://doi.org/10.1007/s11356-020-07829-x>.
- [52] W. Wan, Y. Zhao, S. Wei, C.A. Triana, J. Li, A. Arcifa, C.S. Allen, R. Cao, G. R. Patzke, Mechanistic insight into the active centers of single/dual-atom Ni/Fe-based oxygen electrocatalysts, *Nat. Commun.* 12 (2021) 5589, <https://doi.org/10.1038/s41467-021-25811-0>.